HHS Public Access

Author manuscript

*J Am Chem Soc*. Author manuscript; available in PMC 2024 September 27.

Published in final edited form as:

*J Am Chem Soc*. 2023 September 27; 145(38): 20825–20836. doi:10.1021/jacs.3c04964.

# Tailored chemical reactivity probes for systemic imaging of aldehydes in fibroproliferative diseases

*Corresponding Author Peter Caravan – Athinoula A. Martinos Center for Biomedical Imaging, Institute for Innovation in Imaging (i3), Department of Radiology, Massachusetts General Hospital, Harvard Medical School, Boston, Massachusetts 02129, United States; pcaravan@mgh.harvard.edu.

**Hua Ma –** Athinoula A. Martinos Center for Biomedical Imaging, Institute for Innovation in Imaging (i3), Department of Radiology, Massachusetts General Hospital, Harvard Medical School, Boston, Massachusetts 02129, United States;

**Iris Y. Zhou –** Athinoula A. Martinos Center for Biomedical Imaging, Institute for Innovation in Imaging (i3), Department of Radiology, Massachusetts General Hospital, Harvard Medical School, Boston, Massachusetts 02129, United States;

**Y. Iris Chen –** Athinoula A. Martinos Center for Biomedical Imaging, Institute for Innovation in Imaging (i3), Department of Radiology, Massachusetts General Hospital, Harvard Medical School, Boston, Massachusetts 02129, United States;

**Nicholas J. Rotile –** Athinoula A. Martinos Center for Biomedical Imaging, Institute for Innovation in Imaging (i3), Department of Radiology, Massachusetts General Hospital, Harvard Medical School, Boston, Massachusetts 02129, United States;

**Ilknur Ay –** Athinoula A. Martinos Center for Biomedical Imaging, Institute for Innovation in Imaging (i3), Department of Radiology, Massachusetts General Hospital, Harvard Medical School, Boston, Massachusetts 02129, United States;

**Eman Akam –** Athinoula A. Martinos Center for Biomedical Imaging, Institute for Innovation in Imaging (i3), Department of Radiology, Massachusetts General Hospital, Harvard Medical School, Boston, Massachusetts 02129, United States;

**Huan Wang –** Athinoula A. Martinos Center for Biomedical Imaging, Institute for Innovation in Imaging (i3), Department of Radiology, Massachusetts General Hospital, Harvard Medical School, Boston, Massachusetts 02129, United States;

**Rachel Knipe –** Division of Pulmonary and Critical Care Medicine and the Center for Immunology and Inflammatory Diseases, Massachusetts General Hospital, Boston, Massachusetts 02114, United States;

**Lida P. Hariri –** Division of Pulmonary and Critical Care Medicine and the Center for Immunology and Inflammatory Diseases, Massachusetts General Hospital, Boston, Massachusetts 02114, United States; Department of Pathology, Massachusetts General Hospital, Harvard Medical School, Boston, Massachusetts 02114, United States;

**Caiyuan Zhang –** Athinoula A. Martinos Center for Biomedical Imaging, Institute for Innovation in Imaging (i3), Department of Radiology, Massachusetts General Hospital, Harvard Medical School, Boston, Massachusetts 02129, United States;

**Matthew Drummond –** Division of Pulmonary and Critical Care Medicine and the Center for Immunology and Inflammatory Diseases, Massachusetts General Hospital, Boston, Massachusetts 02114, United States;

**Pamela Pantazopoulos –** Athinoula A. Martinos Center for Biomedical Imaging, Institute for Innovation in Imaging (i3), Department of Radiology, Massachusetts General Hospital, Harvard Medical School, Boston, Massachusetts 02129, United States;

**Brianna Moon –** Athinoula A. Martinos Center for Biomedical Imaging, Institute for Innovation in Imaging (i3), Department of Radiology, Massachusetts General Hospital, Harvard Medical School, Boston, Massachusetts 02129, United States;

**Avery T. Boice –** Athinoula A. Martinos Center for Biomedical Imaging, Institute for Innovation in Imaging (i3), Department of Radiology, Massachusetts General Hospital, Harvard Medical School, Boston, Massachusetts 02129, United States;

**Samantha E. Zygmont –** Athinoula A. Martinos Center for Biomedical Imaging, Institute for Innovation in Imaging (i3), Department of Radiology, Massachusetts General Hospital, Harvard Medical School, Boston, Massachusetts 02129, United States;

**Jonah Weigand-Whittier –** Athinoula A. Martinos Center for Biomedical Imaging, Institute for Innovation in Imaging (i3), Department of Radiology, Massachusetts General Hospital, Harvard Medical School, Boston, Massachusetts 02129, United States;

**Mozhdeh Sojoodi –** Division of Gastrointestinal and Oncologic Surgery, Massachusetts General Hospital, Harvard Medical School, Boston, Massachusetts 02114, United States;

**Romer A. Gonzalez-Villalobos –** Cardiovascular and Metabolism Discovery, Janssen Research and Development LLC, Boston, Massachusetts 02115, United States;

**Michael K. Hansen –** Cardiovascular and Metabolism Discovery, Janssen Research and Development LLC, Boston, Massachusetts 02115, United States;

**Kenneth K. Tanabe –** Division of Gastrointestinal and Oncologic Surgery, Massachusetts General Hospital, Harvard Medical School, Boston, Massachusetts 02114, United States;

Author Contributions

All authorshave contributedto the design and implementationof the studiesreportedhere and have given approvalto thefinal versionof the manuscript.

Supporting Information

The Supporting Information is available free of charge on the ACS Publications website.

Detailed synthesis and characterization data, additional experimental details, materials, methods, and supporting movie.

H.M., E.A., and P.C. are inventors of a filed patent based on the work here (Molecular probes for in vivo detection of aldehydes. PCT/US2022/072310). P.C. has equity in and is a consultant to Collagen Medical LLC, has equity in Reveal Pharmaceuticals Inc., and has research support from Transcode Therapeutics, Pliant Therapeutics, Takeda, and Janssen. L.P.H. reports grants from Boehringer Ingelheim and has received personal consulting fees from Boehringer Ingelheim, Pliant Therapeutics, Bioclinica, and Biogen Idec. R.G.V., and M.K.H. are employed by Janssen. The other authors declare that they have no competing interests.

**Hua Ma**[a], **Iris Y. Zhou**[a], **Y. Iris Chen**[a], **Nicholas J. Rotile**[a], **Ilknur Ay**[a], **Eman A. Akam**[a], **Huan Wang**[a], **Rachel S. Knipe**[b], **Lida P. Hariri**[b,c], **Caiyuan Zhang**[a], **Matthew Drummond**[b], **Pamela Pantazopoulos**[a], **Brianna F. Moon**[a], **Avery T. Boice**[a], **Samantha E. Zygmont**[a], **Jonah Weigand-Whittier**[a], **Mozhdeh Sojoodi**[d], **Romer A. Gonzalez-Villalobos**[e], **Michael K. Hansen**[e], **Kenneth K. Tanabe**[d], **Peter Caravan**[a,*]

[a]Athinoula A. Martinos Center for Biomedical Imaging, Institute for Innovation in Imaging ($i^3$), Department of Radiology, Massachusetts General Hospital, Harvard Medical School, Boston, Massachusetts 02129, United States.

[b]Division of Pulmonary and Critical Care Medicine and the Center for Immunology and Inflammatory Diseases, Massachusetts General Hospital, Boston, Massachusetts 02114, United States.

[c]Department of Pathology, Massachusetts General Hospital, Harvard Medical School, Boston, Massachusetts 02114, United States.

[d]Division of Gastrointestinal and Oncologic Surgery, Massachusetts General Hospital, Harvard Medical School, Boston, Massachusetts 02114, United States

[e]Cardiovascular and Metabolism Discovery, Janssen Research and Development LLC, Boston, Massachusetts 02115, United States.

## Abstract

During fibroproliferation, protein-associated extracellular aldehydes are formed by the oxidation of lysine residues on extracellular matrix proteins to form the aldehyde allysine. Here we report three Mn(II)-based, small molecule magnetic resonance (MR) probes that contain α-effect nucleophiles to target allysine in vivo and report on tissue fibrogenesis. We used a rational design approach to develop turn-on probes with a 4-fold increase in relaxivity upon targeting. The effects of aldehyde condensation rate and hydrolysis kinetics on the performance of the probes to detect tissue fibrogenesis noninvasively in mouse models were evaluated by a systemic aldehyde tracking approach. We showed that for highly reversible ligations, off-rate was a stronger predictor of in vivo efficiency, enabling histologically validated, three-dimensional characterization of pulmonary fibrogenesis throughout the entire lung. The exclusive renal elimination of these probes allowed for rapid imaging of liver fibrosis. Reducing the hydrolysis rate by forming an oxime bond with allysine enabled delayed phase imaging of kidney fibrogenesis. The imaging efficacy of these probes, coupled with their rapid and complete elimination from the body, make them strong candidates for clinical translation.

## Graphical Abstract

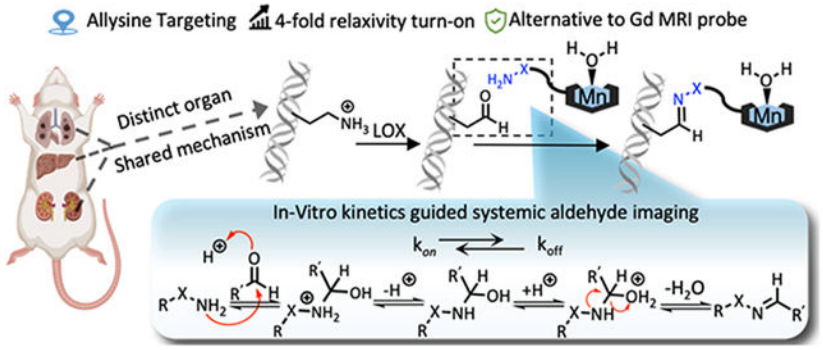


**Keywords**

Molecular imaging; reaction kinetics; fibrosis; magnetic resonance imaging; manganese

## Introduction

Electrophilic carbonyls such as ketones and aldehydes are generally considered rare in mammalian biology, existing at low concentrations in homeostasis and only transiently due to their reactivity in a nucleophilic environment. This is especially true in the extracellular space.[1, 2] Indeed, the scarcity of extracellular carbonyls has led to the development of bioorthogonal conjugation chemistry involving aldehydes. For example, Bertozzi's early work on modifying cell surfaces relied on the integration of keto sialic acid to cell-surface glycans, which then can be covalently ligated by hydrazine or oxyamine under physiological conditions.[3, 4] Paulson and co-workers introduced aldehydes into cell-surface sialic acid residues and then captured the modified glycoproteins by reaction with aminooxybiotin followed by streptavidin chromatography.[5] Taking advantage of the small size and compatibility in living systems, aldehyde/ketone have been utilized as labeling blocks or targeting warheads for bioorthogonal ligation.[6-8]

An important aldehyde in the extracellular matrix (ECM) is the amino acid allysine which is formed by the oxidation of lysine residues by the enzyme lysyl oxidase (LOX) and its paralogs.[9] Allysine formed on collagens (or elastin) undergoes a series of condensation and rearrangement reactions with other collagens that result in irreversible bonds that crosslink the proteins and stabilize the ECM. Outside of development and wound healing, tissue levels of LOX and allysine are low in healthy, mature mammals. However, if the tissue is damaged then LOX is upregulated while the tissue is being remodeled.[10] We have found that lung and liver tissue allysine concentrations can be in the hundreds of micromolar during such pathological processes.[11, 12]

About half of mortality in the industrialized world is caused by a disease that has a fibroproliferative component.[13, 14] Fibrosis is characterized by tissue scarring, and as functional tissue is replaced by scar, the organ becomes less compliant and dysfunctional. When progressive, fibrosis leads to organ failure and/or death. In organs like liver, fibrosis has been shown to promote tumor formation.[15] Many cancers also have a fibrotic component that is believed to promote tumor growth and shield cancer from

chemo- or immunotherapy.[16] Common diseases associated with fibrosis are non-alcoholic steatohepatitis (NASH), [17] chronic kidney disease (CKD),[18] heart failure,[19] but there are also less common fibrotic diseases such as idiopathic pulmonary fibrosis (IPF),[20] and all of them cause significant morbidity and mortality. A major unmet need across all of these diseases is the ability to measure disease activity noninvasively,[21, 22] which could help identify the early onset of disease, could distinguish between an active disease that is progressing from stable scar, could provide prognostic information, or could be used to monitor response to therapy.

The high concentration of allysine during fibrogenesis makes it amenable to detection by a targeted magnetic resonance (MR) probe molecule.[12, 23-26] The general absence of aldehydes in the ECM of healthy tissue suggests that an extracellular, aldehyde-targeted probe would have high specificity for fibroproliferative disease activity. There are several considerations in designing a molecular probe for noninvasive sensing of extracellular aldehydes in the body by MRI.[27] The probe should produce a strong MR signal change and requires an appropriate MR signal generator like a $Gd^{3+}$ or $Mn^{2+}$ chelate. The probe should be metabolically stable in vivo such that the MR signal reflects the distribution of the probe and not metabolites. For liver imaging applications, it is important that the probe not accumulate in the liver or undergo hepatobiliary elimination, as this would increase the background signal. Since MR relaxation probes function by changing the existing MR signal, i.e. they are contrast agents, it is necessary to acquire an image before and after administering the probe to see the signal change induced by the probe. The ideal probe would accumulate rapidly and be retained at its target immediately after injection, but the unbound probe would be rapidly eliminated to minimize nonspecific signal enhancement. Because the dose required for molecular MRI is fairly high (mg metal ion per kg body weight), it is also important that the probe is ultimately eliminated from the body. Finally, since we are targeting extracellular aldehydes, it is important that the probe have an extracellular distribution to minimize any background signal from intracellular aldehydes.

In this study, we describe three novel, extracellular aldehyde targeting probes that comprise a $Mn^{2+}$ chelate conjugated to an aldehyde reactive moiety. As an aldehyde reactive group, we used either alkyl hydrazine, an alpha-carboxylate alkyl hydrazine, and an alpha-carboxylate oxyamine. These designs enabled us to examine the effects of aldehyde condensation rate and condensation product hydrolysis rate on the in vivo performance of the probes for aldehyde sensing in mouse models of lung, liver, and kidney fibrosis.

## Results

### Design and characterization of aldehyde-targeting MR probes.

We designed our probes, Figure 1A, on the symmetric macrocyclic Mn(PC2A)($H_2O$) core which contains one rapidly exchanging coordinated water co-ligand and is thermodynamically stable and kinetically inert with respect to $Mn^{2+}$ dissociation in vivo.[28] The PC2A chelator was readily derivatized at the N7 position to introduce an aldehyde reactive group, either an alkyl hydrazine or oxyamine moiety, as these groups undergo fast reversible condensation reactions with aldehydes. Hydrazines typically have faster aldehyde condensation rates than oxyamines at neutral pH, but the hydrolysis rate of the

resultant hydrazone is much faster than that of an oxime. For the condensation reaction, dehydration of the tetrahedral intermediate is typically the rate-limiting step and the reaction proceeds under general acid catalysis.[29] Substitution of an acidic moiety adjacent to the hydrazine/oxyamine will accelerate the condensation reaction but may also catalyze the back reaction. **MnL1** and **MnL2** allow for the direct comparison between a hydrazine and an oxyamine. **MnL1** and **MnL3** allow for the direct comparison of the effect of the α-carboxylate of reaction kinetics and subsequent in vivo performance. We also compare **MnL2** to the historic compound **GdOA** to assess the effect of the a-carboxylate on oxyamine condensation/hydrolysis kinetics. **MnL4** was synthesized as a structurally matched negative control, which should have similar pharmacokinetic properties as **MnL1**, **MnL2**, and **MnL3**, but is incapable of undergoing condensation with allysine. All the complexes are very hydrophilic which should minimize non-specific protein binding and reduce the fraction of hepatobiliary elimination.

Each of the Mn(II) complexes was synthesized starting from the macrocycle pyclen, followed by regioselective alkylation of the N4 and N10 positions using *tert*-butyl-bromoacetate at pH 8. Next, the N7-position was alkylated with *N*-(3-Bromopropyl)phthalimide, and the primary amine liberated by reaction with hydrazine. This common intermediate was used to prepare each of the Mn(II) probes by conventional amide bond formation with the appropriate synthon to introduce α-carboxylate substituted hydrazine, α-carboxylate substituted oxyamine, terminal hydrazine, or dimethylamine group. After TFA-promoted deprotection and subsequent Mn(II) chelation, we accessed the four Mn(II) probes. The synthetic procedures are fully described in Supporting Information. Each compound was purified and characterized using standard methods (preparative HPLC, $^{1}$H NMR, $^{13}$C NMR, LC-MS, ICP-MS, and LC-ICP-MS; please see Supporting Information for details).

The condensation reaction rate constants with butyraldehyde were measured by UV spectroscopy under pseudo-first-order conditions with respect to each probe. As shown in Figure 1B and S1, introduction of the α-carboxylate moiety led to 3 – 4 fold higher condensation reaction rates: **MnL1** had a second-order rate constant of 12.1 ± 1.9 $M^{-1}s^{-1}$ compared to 4.6 ± 0.3 $M^{-1}s^{-1}$ for **MnL3**; **MnL2** had a second-order rate constant of 2.5 ± 0.2 $M^{-1}s^{-1}$ compared to 0.6 ± 0.1 $M^{-1}s^{-1}$ for **GdOA**. This result confirmed the hypothesis that intramolecular acidic condition would facilitate the condensation reaction between hydrazine/oxyamine and aldehyde. Then, the hydrolysis of hydrazone and oxime products with butyraldehyde were investigated by HPLC. Following Kalia and Raines,[30] we used an excess of formaldehyde to trap the liberated nitrogen base and thereby push the hydrolysis reaction to completion without interference from the reverse (condensation) reaction. As shown in Figure 1C and S2, **MnL1**-hydrazone hydrolysis is 3-times faster than **MnL3**-hydrazone, and **MnL2**-oxime hydrolysis is 5-times faster than **GdOA**. In other words, the α-carboxylate moiety accelerates condensation and hydrolysis to a similar extent. Measurement of the on- and off-rate constants allowed us to compute the dissociation constant ($K_d$) as the ratio $k_{off}/k_{on}$ (Figure 1D). The much slower off-rate of the oxime hydrolysis resulted in 2 orders of magnitude lower $K_d$ for **MnL2** and **GdOA** compared to

**MnL1** and **MnL3**. However, since the a-carboxylate moiety accelerates condensation and hydrolysis equally, there was little difference in $K_d$ between **MnL1** and **MnL3**.

MR probes are characterized by their relaxivity, $r_1$, which is the change in solvent $1/T_1$ caused by adding the probe, normalized to the probe concentration. We measured relaxivity (1.4 T, 37 °C, pH 7.4) of each complex in phosphate-buffered saline (PBS) and then again in PBS containing bovine serum albumin (BSA). The four Mn complexes exhibited similar $r_1$ values (about 3.1 $mM^{-1}s^{-1}$) in PBS, consistent with one coordinated water ligand (Figure 1E). The presence of a single coordinated water co-ligand was confirmed by temperature-dependent $H_2{}^{17}O$ transverse relaxation rates using the method of Gale et al. (Figure S3).[31] In the presence of excess BSA there was little to no relaxivity enhancement, indicating low nonspecific protein binding. We next measured the relaxivity of each complex in the presence of oxidized BSA wherein about 4 lysine side chains on BSA were oxidized to allysine, and we used this allysine-modified BSA (BSA-Ald, 21.9 mg $mL^{-1}$, 0.6 mM aldehyde) as water-soluble model aldehyde bearing protein.[32, 33] In the presence of BSA-Ald (3 h incubation, 37°C), the relaxivity increased by 90%, 150%, 150%, 100%, and 10% (5.9 $mM^{-1}s^{-1}$, 7.9 $mM^{-1}s^{-1}$, 7.7 $mM^{-1}s^{-1}$, 8.2 $mM^{-1}s^{-1}$, and 3.6 $mM^{-1}s^{-1}$) for **MnL1**, **MnL2**, **MnL3**, **MnL4**, and **GdOA**, respectively, relative to their relaxivity values in PBS. We then separated the unbound probe from the BSA-Ald bound probe by ultrafiltration with a molecular weight cutoff filter (Figure S4) and then measured the relaxivity of the protein-bound species. The protein-bound relaxivities were 4 times higher than the relaxivity of the unbound probe (12.7 $mM^{-1}s^{-1}$, 13.6 $mM^{-1}s^{-1}$, 12.7 $mM^{-1}s^{-1}$, and 17.6 $mM^{-1}s^{-1}$ for **MnL1**, **MnL2**, **MnL3**, and **GdOA** respectively). In comparison, the relaxivities of non-reactive control probe **MnL4** were practically unchanged from PBS to BSA or BSA-Ald, indicating a lack of protein binding for the control probe. At a higher magnetic field of 4.7 T where the imaging studies were performed, the relaxivity of BSA-Ald bound probes was also significantly enhanced compared to the unbound form (113% increase for **MnL1**, 115% increase for **MnL2**, 115% increase for **MnL3**, Figure S5).

The thermodynamic stability constant of $Mn^{2+}$ with the unmodified PC2A ligand was reported to be log $K_{MnPC2A}$ = 17.09,[28] and we expect similar stability with the complexes here. We assessed the kinetic inertness of the 4 Mn complexes described here by transmetalation experiments with an excess of $Zn^{2+}$, which should form more stable complexes than $Mn^{2+}$ based on its position in the Irving-Williams series.[34] The Mn(II) complexes were incubated with 25 equivalents of $Zn^{2+}$ at 37 °C, in pH 6.0 MES buffer, and changes in the paramagnetic longitudinal relaxation rate ($\%R_1{}^P$) were used as readout. Under this condition, any free $Mn^{2+}$ released by chelator will cause an increase in $R_1{}^P$ owing to the higher relaxivity of the $Mn^{2+}$ aqua ion. Mn-PyC3A, which is currently being developed as an MRI probe and was shown to be excreted from animals in its intact form, was measured as a comparative benchmark.[35] Measured pseudo-first-order rate constants were 2.5 ± 0.1 × $10^{-4}$, 2.4 ± 0.3 ×$10^{-4}$, 2.3 ± 0.3 ×$10^{-4}$, 2.2 ± 0.4 ×$10^{-4}$, and 5.5 ± 0.4 ×$10^{-4}$ $s^{-1}$ for **MnL1**, **MnL2**, **MnL3**, **MnL4**, and Mn-PyC3A, respectively (Figure S6). Since the Mn-PC2A derivatives reported here are twice as inert as Mn-PyC3A, we expect these complexes to also be stable in vivo with respect to $Mn^{2+}$ dissociation.

The stabilities of **MnL1**, **MnL2**, **MnL3**, and **MnL4** in human plasma were also assessed using HPLC coupled to ICP-MS (LC-ICP-MS) to measure the formation of any new Mn-containing species (Figure S7). Incubation of 1.0 mM complex in human plasma at 37 °C for 1 h resulted in the formation of up to 18 % of new Mn-containing species for **MnL1**, up to 5% for **MnL2**, and up to 5% for **MnL3**, but no new Mn-containing species were observed when **MnL4** was incubated with plasma. Since no new species were observed with the control probe, it is likely that the species formed in plasma are products of reactions with endogenous aldehyde or ketone-containing molecules.

### Distribution and pharmacokinetics in mice.

We next used MRI and positron emission tomography (PET) to evaluate the distribution, pharmacokinetics, and whole-body elimination of the probes in naïve C57Bl/6 mice. As shown in Figure S8A, intravenous (i.v.) administration of 0.1 mmol•kg$^{-1}$ of either **MnL1**, **MnL2**, **MnL3**, or **MnL4** resulted in an immediate and marked increase in MR signal in the blood pool (aorta). We measured the percentage change in signal intensity (%SI) over time in the aorta, liver, and kidney and the data were fit with a monoexponential decay function to obtain the half-life of the probe in each tissue (Figure S8 B-D). All four probes displayed rapid and almost identical blood clearance with blood half-lives of 7.1 ± 1.2 min (**MnL1**), 7.0 ± 1.4 min (**MnL2**), 7.1 ± 1.0 min (**MnL3**), and 7.2 ± 0.9 min (**MnL4**). All probes were eliminated from the body via the kidneys. Only minimal and transient liver enhancement was observed and matched the blood pool kinetics. To measure whole-body elimination, we radiolabeled each probe with the Mn-52 isotope and performed PET imaging and ex vivo biodistribution analysis 24 h post-injection of each probe in naïve C57Bl/6 mice. The high sensitivity of PET allows us to detect any trace levels of injected Mn-probe in the body and to distinguish the distribution and elimination of injected probe from endogenous Mn. Mice were injected a dose of **MnL1**, **MnL2**, **MnL3** or **MnL4** (0.1 mmol•kg$^{-1}$) mixed with $^{52}$**MnL1**, $^{52}$**MnL2**, $^{52}$**MnL3**, or $^{52}$**MnL4** respectively (1.0 – 1.2 MBq, Figure S9) by intravenous injection and simultaneous PET-MRI was performed 24 h post-injection (Figure S10A). Finally, the organs were harvested for ex vivo biodistribution analysis. Data are presented as percentage injected dose per gram organ (%ID/g, Figure S10B). At 24 h post-injection, >96% of the injected Mn is eliminated from the mice (98.5% for **MnL1**, 96.3% for **MnL2**, 98.6% for **MnL3**, and 99.0% for **MnL4**). PET-MRI 24 h post-injection showed that most of the remaining activity was localized in the kidneys for each probe, except for **MnL2** where we also observed signal in the skin. The skin is an organ with elevated LOX family expression as a result of the rapid turnover,[36, 37] given the much higher hydrolytic stability of the oxime bond, the higher retained activity from **MnL2** is most likely due to binding to intrinsic allysine. An important observation in the PET study for all compounds was the absence of Mn-52 activity in the liver, lymph nodes, bone, brain, and salivary glands of the mice, which would have been indicative of dechelated Mn-52, suggesting that these complexes remain intact in vivo.[38]

### Comparison of noninvasive aldehyde sensing in a mouse model of pulmonary fibrogenesis.

We next sought to compare the effects of differing on- and off-rates on noninvasive aldehyde sensing in vivo. We first used a bleomycin-induced lung fibrosis mouse model (BM, Figure S11). A single intratracheal (i.t.) dose of bleomycin results in rapid development of pulmonary fibrosis in mice, and we have previously shown that fibrogenesis and lung allysine levels peak at 14 days post injury.[39] Compared to naïve mice, bleomycin injury resulted in distorted lung architecture and increased cellular infiltration on hematoxylin and eosin (H&E) staining (Figure 2A), while Masson's trichrome staining revealed large regions of fibrosis (blue staining of collagen, Figure 2B). Biochemical quantification of allysine showed a 2-fold increase in the content of this aldehyde in the BM-injured lungs (Figure 2C) and collagen lung concentration as quantified by hydroxyproline (Figure 2D), was also significantly elevated 1.3-fold.

As shown in Figure 2 E, F and S12, from 10 min to 60 min post-injection, lung signal enhancement, expressed as the change in the lung signal to muscle signal ratio (ΔLMR), all four probes exhibited similar and rapid decreases in naïve mice, demonstrating fast elimination of the probes from normal lungs. In BM mice, the non-binding probe **MnL4** produced higher ΔLMR at 10 min post-injection compared to naïve mice, demonstrating an increased extracellular volume in BM-injured lungs. The **MnL4** signal enhancement then exhibited fast decay. In comparison, higher and persistent contrast enhancement was observed in BM mice injected with hydrazine/oxyamine bearing probes, with significantly higher ΔLMR than in naïve mice and significantly higher ΔLMR than that of **MnL4** in BM mice 60 min post-injection (Figure 2G). Notably, the signal enhancement of **MnL1** and **MnL3** in fibrotic lung kept decreasing from 10 min to 110 min post-injection, while the more hydrolytically stable **MnL2** showed ΔLMR reaching a plateau at 60 min post-injection and then remaining stable.

Interestingly, **MnL3** exhibited superior signal enhancement compared to **MnL1**, which was confirmed by pairwise comparison in the same mice to mitigate the inter-animal heterogeneity of this model (Figure 2H). **MnL1** and **MnL3** had similar equilibrium constants with aldehyde but different condensation and hydrolysis rates. Therefore, the greater ΔLMR with **MnL3** than **MnL1** could be attributed to a slower off-rate with **MnL3**. We also measured the lung half-life ($T_{1/2}$) of each probe by fitting the change in ΔLMR with time (Figure 2I, S13). We found that both **MnL1** and **MnL3** had significantly longer $T_{1/2}$ in BM mice compared with naïve mice or compared with **MnL4** in BM mice. In BM mice, **MnL3** exhibited a significantly slower washout than **MnL1** ($T_{1/2}$ = 41.5 ± 6.3 min vs. 33.6 ± 5.1 min, P = 0.003), likely due to the greater hydrolytic stability of **MnL3**. **MnL2**, which forms a stable oxime bond, showed a very long $T_{1/2}$ value that could not be determined based on the 2-hour imaging study.

Ex vivo determination of lung Mn content at 60 min post-injection of **MnL1**, **MnL2**, and **MnL3** was significantly elevated in BM mice compared to naïve mice and significantly elevated compared to **MnL4** administered to naïve or BM mice, in line with the findings from in vivo MRI (Figure 2J). The MRI signal enhancement was highly correlated ($R^2$ >

0.84) with lung allysine content (Figure 2K). The slope of ΔLMR vs allysine concentration was higher for **MnL3** (0.015) than for **MnL1** (0.011) indicating that **MnL3** was 40% more sensitive in detecting fibrogenesis. The ΔLMR values also significantly correlated with hydroxyproline content in lungs for each of the three aldehyde-targeted probes (Figure S14).

### Noninvasive three-dimensional mapping of fibrogenesis.

IPF has a complex phenotype that is manifested by clinical, etiologic, and molecular heterogeneity. In fact, heterogeneity in the radiographic and pathologic features of usual interstitial pneumonia is required for the definitive diagnosis of IPF.[40] However, mapping lung fibrogenesis heterogeneity remains challenging with lung biopsy and other diagnostic modalities. The bleomycin-induced pulmonary fibrogenesis model exhibited strong heterogeneity mimicking the clinical condition. To validate the molecular MRI-based mapping of fibrogenesis with ex vivo histology BM mice were imaged pre- and 40 min post-injection of **MnL3**, and the %SI enhancement in each pixel was computed to generate a 3D signal enhancement (%SI) map representing the location and extent of fibrotic regions (Figure 3A, B and Movie S1). Following imaging, the injured lung was harvested, fixed, serially sectioned, and stained with Masson's trichrome for the presence of fibrosis (blue staining, Figure 3C). We next segmented the blue color in the serial histology images and generated a fibrosis density map for comparison with the corresponding MR %SI map in Figure 3D; the rest of mice can be seen in Figure S15. From the histological representation of fibrosis density, we found the upper-right lobe (dashed line) of this lung exhibited severe fibrotic disease, followed by left lobe (dot-and-dash line), while the lower-right lobe was less fibrotic. Consistently, the corresponding MRI map exhibited a similar pattern of signal enhancement after the injection of the fibrogenesis-sensing probe **MnL3**. These results demonstrate how **MnL3**-based molecular MRI can noninvasively track whole lung fibrosis disease activity, and potentially replace, or complement conventional invasive lung histology.

### MnL1 detection of liver fibrogenesis.

After confirming the specificity of **MnL1** in targeting fibrogenesis in the lung, we then tested whether **MnL1**-enhanced MRI could detect liver fibrogenesis in a toxin-induced fibrosis model. Carbon tetrachloride ($CCl_4$) is a well-established toxin that when administered repeatedly results in liver fibrosis and ultimately hepatocellular carcinoma.[39] In this study, liver fibrosis was induced in 8-week-old male C57BL/6 mice by oral gavage of 40% $CCl_4$ diluted in olive oil for 12 weeks, and vehicle-treated mice were used as controls. Figure 4A shows that **MnL1** administration rapidly produced a significant liver signal enhancement in $CCl_4$-treated mice but not in control mice. Change in the liver-to-muscle contrast to noise ratio (ΔCNR) was higher in $CCl_4$-treated mice, while the liver only transiently enhanced in vehicle-treated control mice (Figure 4B). ΔCNR was 3-fold higher at 20 minutes post-injection, and the area under the ΔCNR curve was significantly larger in $CCl_4$ treated mice than in vehicle-treated mice (Figure 4C), demonstrating the potential for imaging liver fibrogenesis with **MnL1**.

### Superior hydrolytic stability of the oxime bond enables molecular MR of renal fibrogenesis.

Molecular imaging of the kidney is particularly challenging because almost all probes are eliminated to some extent through the kidneys, resulting in a high background signal. To achieve specific molecular imaging of the kidneys, one must wait sufficient time for the nonspecific background renal signal to diminish and the probe must remain bound to its target for this extended period. Here we tested whether the oxyamine probe **MnL2** could be used to detect renal fibrosis. We also sought to test whether the 4-fold higher condensation rate constant for **MnL2** compared to a previously reported probe **GdOA** would result in greater signal enhancement in fibrotic kidney.

We used a unilateral renal ischemia-reperfusion injury (IRI) mouse model (Figure S16) where one kidney is clamped and then reperfused. This results in initial inflammation and cell death that then gives way to tissue fibrosis.[41] We evaluated mice at 14 days after IRI and demonstrated fibrosis in both the renal cortex and medulla by histology (Figure 5A) and by quantifying the biochemical biomarker hydroxyproline (Figure 5B). Figure 5A shows obvious collagen deposition in the cortex and medulla of the IRI kidney, but not in the healthy kidney. Consistent with histological staining, hydroxyproline concentrations in the IRI kidney were significantly higher than in the healthy kidney for both cortex and medulla (3.1-times higher than the cortex of healthy kidney; 2.8-times higher than the medulla of the healthy kidney; $p < 0.001$). Lysyl oxidase like 1 (LOXL 1) and LOXL 2 enzymes are both upregulated in the IRI kidney (Figure S17)

We measured kidney T1 values at 9.4 T prior to and 4 hours after injecting the probe. In naïve mice, both probes were effectively eliminated from the kidneys by 4 h post-injection (Figure 5C). We computed T1 maps on a pixel basis and then measured the mean R1 (R1 = 1/T1) for cortex and medulla, respectively. We then calculated the change in relaxation rate ($\Delta R1 = R1_{Post} - R1_{Pre}$) induced by the probe as a measure of probe concentration in that tissue. As shown in Figure 5D and E, in both cortex and medulla of the IRI kidney, ΔR1 after **MnL2** injection was significantly higher than for those regions of healthy kidneys. Using **GdOA**, we also observed significantly larger ΔR1 in the injured kidney compared to healthy mice, demonstrating that both oxyamine-containing probes can be used to image renal fibrogenesis. These findings were supported by ex vivo quantification of gadolinium and manganese in these tissues (Figure S18). In comparing the in vivo performance of **MnL2** and **GdOA**, the increase in ΔR1 was 30% higher for **MnL2** in the cortex of the IRI kidney than **GdOA** and was 40% higher than **GdOA** in the medulla. This result demonstrated that the 4-fold higher condensation rate constant with **MnL2** translated into improved in vivo performance for detection of renal fibrogenesis.

Here we used a unilateral IRI model and thus the contralateral kidney, which did not undergo IRI served as an internal control to the IRI kidney. We performed intra-animal comparisons between ΔR1 in the contralateral kidney and the IRI kidney for **MnL2** and **GdOA** (Figure S19). For **GdOA**, ΔR1 was significantly higher in the IRI medulla compared to the contralateral medulla ($p < 0.001$), but there was no significant difference in the renal cortex. For **MnL2**, on the other hand, ΔR1 was significantly increased in the cortex and

medulla of the IRI kidney compared to those regions in the contralateral kidney ($p = 0.03$ for cortex; $p = 0.003$ for medulla).

## Discussion

Fibrosis-related diseases present an enormous burden to society. These diseases range from myocardial infarction and hypertrophic cardiomyopathy in the heart,[19] to Crohn's disease in the intestine,[42] to scleroderma in the skin.[43] IPF is a progressive fibrosing disease of the lung with worse outcomes than many types of cancers.[44] NASH is a chronic liver disease that afflicts approximately 5% of the population in the United States and can lead to cirrhosis, liver failure, primary liver cancer, and/or death.[16, 45] Chronic kidney disease (CKD) is a progressive disease that ultimately leads to renal failure.[18] All these diseases present unmet diagnostic challenges for example in improved early diagnosis, improved prognostication, and monitoring treatment and disease progression. A noninvasive test that could address some or all these needs would be expected to have an enormous impact.

To address this unmet need, we designed molecular probes that target the extracellular aldehyde allysine, which is increased during fibrogenesis. We used MR imaging because of its ability to image any organ in the body with three-dimensional high-resolution images and its operator-independent characteristic. In addition, MR imaging does not require ionizing radiation, which is particularly important for chronic diseases where patients may require multiple imaging exams over their lifetime. We designed small, hydrophilic probes that do not exhibit appreciable nonspecific protein binding to promote rapid renal elimination and minimize hepatobiliary elimination. The lack of hepatobiliary elimination provided a low background in the liver to enable liver imaging applications.

The three aldehyde-targeting Mn(II) probes had similar properties with respect to relaxivity, water exchange kinetics, and kinetic stability of the Mn(II)-PC2A chelate. The relaxivities of **MnL1**, **MnL2**, and **MnL3** were relatively low (3.1 $mM^{-1}s^{-1}$) when measured in PBS but exhibited a 4-fold turn-on in relaxivity when bound to aldehyde modified BSA at 1.4 T. Importantly, the relaxivity increase was negligible in unmodified BSA, indicating that these compounds do not exhibit appreciable nonspecific protein binding. In a $Zn^{2+}$ challenge assay, the Mn probes were about twice as inert to transmetalation as the complex Mn-PyC3A, which has been evaluated in several animal models and is currently undergoing clinical trials. These stable, hydrophilic Mn(II) probes also exhibited similar pharmacokinetic behavior in healthy mice: rapid renal elimination with blood elimination half-lives typical of compounds with no protein binding; exclusive renal elimination; and nearly complete elimination of injected Mn from the body after 24 hours.

The probes differed however in their kinetics of condensation with aldehydes and hydrolysis of the resultant hydrazone or oxime bond. All three probes bind specifically to fibrogenic injured mouse lung in vivo. However, lung MR signal enhancement appears to depend on a balance of on- and off-rates. The α-carboxy hydrazine bearing **MnL1** exhibited the highest condensation rate constant, but its fibrotic lung-enhancing properties were significantly inferior to **MnL3** which lacked the α-carboxy group. On the other hand, the hydrolysis rate constant for the **MnL3** hydrazone was 3-fold lower than the **MnL1** hydrazone suggesting

that off-rate may be a better predictor of in vivo performance. The α-carboxy oxyamine bearing **MnL2** probe had a hydrolysis rate constant that was 3 orders of magnitude smaller than **MnL3**, but also a 2-fold lower condensation rate constant than **MnL3**. For the first 30 min after injection, the fibrotic lung signal enhancement with **MnL3** was significantly greater than that with **MnL2**, perhaps indicating that signal enhancement will increase with increasing on-rate provided that the back reaction is relatively slow. Interestingly by 2 h post-injection, the fibrotic lung signal enhancement from **MnL3** has diminished as the probe was washed out of the tissue, but the lung enhancement with **MnL2** has reached a plateau owing to the slow hydrolysis of the oxime bond.

For applications, these probes offer different options to characterize the fibroproliferative disease. The hydrazine-based probe **MnL3** enables specific imaging of fibrogenesis shortly after intravenous administration. The relatively fast hydrolysis of the hydrazone, compared to an oxime, results in the elimination of the probe from the body after the imaging study is performed. We showed here that **MnL3**-enhanced MRI of the lung allows for three-dimensional characterization of pulmonary fibrogenesis throughout the entire lungs. Pulmonary fibrosis can affect any part of the lungs – upper or lower, right or left, subpleural or mid lung – and methods that assess the whole lungs are needed. Clinical techniques like high-resolution computed tomography (HRCT) can report on the distribution of advanced fibrosis throughout the whole lungs, but HRCT does not report disease activity.[46] Lung biopsy provides rich data but only samples a single, very small region of the lung that may not be reflective of the whole lung and is a procedure that carries the risk of complications and mortality.[47] Endobronchial optical coherence tomography provides high-resolution images of specific lung regions but again does not report on disease activity.[48]

We also showed that **MnL1**-enhanced MR could detect and quantify liver fibrogenesis within 20 minutes post-injection. In chronic liver diseases like NASH, ultrasound elastography or MR elastography or serum biomarker panels have shown value in detecting the presence of advanced fibrosis.[49] However, these methods are insensitive to detecting fibrosis at earlier stages and do not assess fibrotic disease activity.[50] Prior work in animal models showed that imaging liver fibrogenesis may enable the detection of the earliest stages of liver fibrosis and that imaging disease activity can provide an early readout of response to therapy.[12]

Extending molecular imaging of fibrosis/fibrogenesis to the kidneys is particularly challenging because of the high nonspecific renal signal enhancement as the probe clears through the kidneys. Furthermore, many molecular probes, especially peptide-based probes, are retained in the kidneys. In the **MnL2**-enhanced MR study of pulmonary fibrosis, we found that the lung signal reached a plateau and that we could not estimate a washout rate of **MnL2** from the fibrotic lung over two hours period because the lung signal was not changing. This finding led us to test whether this in vivo hydrolytic stability could be exploited for delayed imaging of the kidney. Our results showed that **MnL2** could indeed be used to specifically detect renal fibrosis in IRI model by imaging the mice before and 4 hours post intravenous injection of **MnL2**. Using T1 mapping, we could accurately quantify fibrogenesis throughout the kidney and segment disease within the cortex and medulla. We also showed that the faster on-rate with **MnL2** compared to **GdOA** resulted in greater MR

signal enhancement in diseased tissue, again demonstrating the importance of optimizing the reactivity of these probes toward aldehydes.

We previously reported a type I collagen targeted PET probe for imaging pulmonary fibrosis,[51, 52] and an aldehyde reactive probe for imaging fibrogenesis.[53] Both of those probes showed significantly higher PET signal in bleomycin injured mouse lungs compared to healthy lungs. It is challenging to directly compare the imaging data obtained with PET to the molecular MR data obtained here because of the differences between the modalities. For MRI, two sets of images must be acquired - before and after probe injection - and then the difference between these images is compared, with the image signal intensity being strongly dependent on both the image acquisition parameters and the relaxivity of the probe when bound to its target, but for PET only a single post-injection image is acquired. Compared to MR probes, microdosing with PET carries the benefit of not requiring extensive preclinical safety and toxicology studies which allows quicker and cheaper advancement into initial clinical trials, and indeed the collagen targeted probe 68Ga-CBP8 is currently being evaluated in several human clinical trials.[54, 55] However MR has many advantages compared to PET: an order of magnitude higher spatial resolution that allows for better delineation of the borders of the lungs and for delineating lung from blood vessels; lack of ionizing radiation; a shelf-stable probe that doesn't need to be prepared on a daily basis; and a much higher availability of MRI scanners compared to PET scanners. For these reasons, the MR probes reported here hold strong potential for clinical translation.

## Conclusion

This study provides insight into the design of molecular MR probes for noninvasive sensing of extracellular aldehydes and how they might be deployed to characterize human diseases. These probes have a high potential for clinical translation given the straightforward syntheses that are amenable to scale-up. While we did not assess the safety and toxicology of the probes, we note that their lack of nonspecific protein binding, lack of cellular uptake in vivo, rapid renal elimination, and whole-body elimination of injected Mn are all favorable properties that should limit the potential for adverse effects. We showed that the probes exhibit a 4-fold increase in relaxivity upon binding to protein containing aldehyde at 1.4 T, near the frequently used clinical field strength of 1.5 T. Our animal experiments were performed at 4.7 T and 9.4 T where the turn-on effect is much lower, e.g. 2-fold increase at 4.7 T. Thus, we expect the signal enhancement in clinical scanners to be higher than what we measured here. While we demonstrated the utility of these probes in mouse models of lung, liver, and kidney disease, such probes would likely prove valuable in other fibroproliferative diseases, including the heart, intestines, blood vessels, skin, etc.

## Supplementary Material

Refer to Web version on PubMed Central for supplementary material.

## ACKNOWLEDGMENT

This work was supported by grants from the National Institutes of Health to P.C. (DK104302, DK121789, HL154125, OD028499, OD032138, OD025234, and OD023503), to E.A. (K01HL155237), to R.K.

(K08HL140175) and by a Sponsored Research Agreement with Janssen. We thank Alana Ross for assistance with the biodistribution study.

## REFERENCES

(1). Prescher JA; Bertozzi CR Chemistry in living systems. Nat. Chem. Biol 2005, 1 (1), 13–21. [PubMed: 16407987]

(2). Shieh P; Bertozzi CR Design strategies for bioorthogonal smart probes. Organic & biomolecular chemistry 2014, 12 (46), 9307–9320. [PubMed: 25315039]

(3). Hang HC; Bertozzi CR Ketone isosteres of 2-N-acetamidosugars as substrates for metabolic cell surface engineering. J. Am. Chem. Soc 2001, 123 (6), 1242–1243. [PubMed: 11456684]

(4). Mahal LK; Yarema KJ; Bertozzi CR Engineering chemical reactivity on cell surfaces through oligosaccharide biosynthesis. Science 1997, 276 (5315), 1125–1128. [PubMed: 9173543]

(5). Zeng Y; Ramya T; Dirksen A; Dawson PE; Paulson JC High-efficiency labeling of sialylated glycoproteins on living cells. Nat. Methods 2009, 6 (3), 207–209. [PubMed: 19234450]

(6). Sletten EM; Bertozzi CR Bioorthogonal chemistry: fishing for selectivity in a sea of functionality. Angew. Chem., Int. Ed 2009, 48 (38), 6974–6998.

(7). Reja RM; Wang W; Lyu Y; Haeffner F; Gao J Lysine-targeting reversible covalent inhibitors with long residence time. J. Am. Chem. Soc 2022, 144 (3), 1152–1157. [PubMed: 35040658]

(8). Aronoff MR; Hiebert P; Hentzen NB; Werner S; Wennemers H Imaging and targeting LOX-mediated tissue remodeling with a reactive collagen peptide. Nat. Chem. Biol 2021, 17 (8), 865–871. [PubMed: 34253910]

(9). Vallet SD; Ricard-Blum S Lysyl oxidases: from enzyme activity to extracellular matrix cross-links. Essays Biochem. 2019, 63 (3), 349–364. [PubMed: 31488698]

(10). Cai L; Xiong X; Kong X; Xie J The role of the lysyl oxidases in tissue repair and remodeling: a concise review. Tissue Eng. Regener. Med 2017, 14 (1), 15–30.

(11). Waghorn PA; Oliveira BL; Jones CM; Tager AM; Caravan P High sensitivity HPLC method for determination of the allysine concentration in tissue by use of a naphthol derivative. J. Chromatogr. B: Anal. Technol. Biomed. Life Sci 2017, 1064, 7–13.

(12). Ning Y; Zhou IY; Roberts JD Jr; Rotile NJ; Akam E; Barrett SC; Sojoodi M; Barr MN; Punshon T; Pantazopoulos P Molecular MRI quantification of extracellular aldehyde pairs for early detection of liver fibrogenesis and response to treatment. Sci. Transl. Med 2022, 14 (663), eabq6297. [PubMed: 36130015]

(13). Friedman SL; Sheppard D; Duffield JS; Violette S Therapy for fibrotic diseases: nearing the starting line. Sci. Transl. Med 2013, 5 (167), 167sr161–167sr161.

(14). Rockey DC; Bell PD; Hill JA Fibrosis—a common pathway to organ injury and failure. N. Engl. J. Med 2015, 372 (12), 1138–1149. [PubMed: 25785971]

(15). Dhar D; Baglieri J; Kisseleva T; Brenner DA Mechanisms of liver fibrosis and its role in liver cancer. Exp. Biol. Med 2020, 245 (2), 96–108.

(16). Valkenburg KC; De Groot AE; Pienta KJ Targeting the tumour stroma to improve cancer therapy. Nat. Rev. Clin. Oncol 2018, 15 (6), 366–381. [PubMed: 29651130]

(17). Pellicoro A; Ramachandran P; Iredale JP; Fallowfield JA Liver fibrosis and repair: immune regulation of wound healing in a solid organ. Nat. Rev. Immunol 2014, 14 (3), 181–194. [PubMed: 24566915]

(18). Liu Y. Cellular and molecular mechanisms of renal fibrosis. Nat. Rev. Nephrol 2011, 7 (12), 684–696. [PubMed: 22009250]

(19). Segura AM; Frazier O; Buja LM Fibrosis and heart failure. Heart Failure Rev. 2014, 19 (2), 173–185.

(20). Martinez FJ; Collard HR; Pardo A; Raghu G; Richeldi L; Selman M; Swigris JJ; Taniguchi H; Wells AU Idiopathic pulmonary fibrosis. Nat. Rev. Dis. Prim 2017, 3 (1), 1–19.

(21). Manning DS; Afdhal NH Diagnosis and quantitation of fibrosis. Gastroenterology 2008, 134 (6), 1670–1681. [PubMed: 18471546]

(22). Popov Y; Schuppan D Targeting liver fibrosis: strategies for development and validation of antifibrotic therapies. Hepatology 2009, 50 (4), 1294–1306. [PubMed: 19711424]

(23). Waghorn PA; Jones CM; Rotile NJ; Koerner SK; Ferreira DS; Chen HH; Probst CK; Tager AM; Caravan P Molecular Magnetic Resonance Imaging of Lung Fibrogenesis with an Oxyamine-Based Probe. Angew. Chem., Int. Ed 2017, 129 (33), 9957–9960.

(24). Akam EA; Abston E; Rotile NJ; Slattery HR; Zhou IY; Lanuti M; Caravan P Improving the reactivity of hydrazine-bearing MRI probes for in vivo imaging of lung fibrogenesis. Chem. Sci 2020, 11 (1), 224–231. [PubMed: 32728411]

(25). Dang T; Suchy M; Truong YJ; Oakden W; Lam WW; Lazurko C; Facey G; Stanisz GJ; Shuhendler AJ Hydrazo-CEST: Hydrazone-Dependent Chemical Exchange Saturation Transfer Magnetic Resonance Imaging Contrast Agents. Chem. - Eur. J 2018, 24 (36), 9148–9156. [PubMed: 29645309]

(26). Brun EMSP-T; Calvert ND; Suchý M; Kirby A; Melkus G; Garipov R; Addison CL; Shuhendler AJ Mapping vitamin B 6 metabolism by hydrazoCEST magnetic resonance imaging. Chem. Commun 2021, 57 (83), 10867–10870.

(27). Wahsner J; Gale EM; Rodríguez-Rodríguez A; Caravan P Chemistry of MRI contrast agents: current challenges and new frontiers. Chem. Rev 2018, 119 (2), 957–1057. [PubMed: 30350585]

(28). Botár R; Molnár E; Trencsényi G. r.; Kiss J; Kálmán FK; Tircsó G Stable and inert Mn (II)-based and pH-responsive contrast agents. J. Am. Chem. Soc 2020, 142 (4), 1662–1666. [PubMed: 31927927]

(29). Kölmel DK; Kool ET Oximes and hydrazones in bioconjugation: mechanism and catalysis. Chem. Rev 2017, 117 (15), 10358–10376. [PubMed: 28640998]

(30). Kalia J; Raines RT Hydrolytic stability of hydrazones and oximes. Angew. Chem., Int. Ed 2008, 47 (39), 7523–7526.

(31). Gale EM; Zhu J; Caravan P Direct measurement of the Mn(II) Hydration state in metal complexes and metalloproteins through 17O NMR line widths. J. Am. Chem. Soc 2013, 135 (49), 18600–18608. [PubMed: 24088013]

(32). Levine RL Oxidative modification of glutamine synthetase. II. Characterization of the ascorbate model system. J. Biol. Chem 1983, 258 (19), 11828–11833. [PubMed: 6137484]

(33). Chao C-C; Ma Y-S; Stadtman ER Modification of protein surface hydrophobicity and methionine oxidation by oxidative systems. Proc. Natl. Acad. Sci 1997, 94 (7), 2969–2974. [PubMed: 9096330]

(34). Leussing D. The estimation of the stabilities of bivalent transition metal complexes and deviations from the irving-williams order. Talanta 1960, 4 (4), 264–267.

(35). Zhou IY; Ramsay IA; Ay I; Pantazopoulos P; Rotile NJ; Wong A; Caravan P; Gale EM Positron Emission Tomography–Magnetic Resonance Imaging Pharmacokinetics, In Vivo Biodistribution, and Whole-Body Elimination of Mn-PyC3A. Invest. Radiol 2021, 56 (4), 261–270. [PubMed: 33136686]

(36). Zhao X; Kwan JYY; Yip K; Liu PP; Liu F-F Targeting metabolic dysregulation for fibrosis therapy. Nat. Rev. Drug. Discov 2020, 19 (1), 57–75. [PubMed: 31548636]

(37). Hayashi K; Fong KS; Mercier F; Boyd CD; Csiszar K; Hayashi M Comparative immunocytochemical localization of lysyl oxidase (LOX) and the lysyl oxidase-like (LOXL) proteins: changes in the expression of LOXL during development and growth of mouse tissues. J. Mol. Histol 2004, 35 (8), 845–855. [PubMed: 15609098]

(38). Graves SA; Hernandez R; Fonslet J; England CG; Valdovinos HF; Ellison PA; Barnhart TE; Elema DR; Theuer CP; Cai W Novel preparation methods of 52Mn for immunoPET imaging. Bioconjugate Chem. 2015, 26 (10), 2118–2124.

(39). Chen HH; Waghorn PA; Wei L; Tapias LF; Schühle DT; Rotile NJ; Jones CM; Looby RJ; Zhao G; Elliott JM Molecular imaging of oxidized collagen quantifies pulmonary and hepatic fibrogenesis. JCI insight 2017, 2 (11).

(40). Albert RK; Schwartz DA Revealing the secrets of idiopathic pulmonary fibrosis. N. Engl. J. Med 2019, 380 (1), 94–96. [PubMed: 30601735]

(41). Furuichi K; Gao J-L; Murphy PM Chemokine receptor CX3CR1 regulates renal interstitial fibrosis after ischemia-reperfusion injury. Am. J. Pathol 2006, 169 (2), 372–387. [PubMed: 16877340]

(42). Li C; Kuemmerle JF Mechanisms that mediate the development of fibrosis in patients with Crohn's disease. Inflamm. Bowel Dis 2014, 20 (7), 1250–1258. [PubMed: 24831560]

(43). Varrica C; Dias HS; Reis C; Carvalheiro M; Simões S Targeted delivery in scleroderma fibrosis. Autoimmun. Rev 2021, 20 (2), 102730. [PubMed: 33338593]

(44). Wu B; Sodji QH; Oyelere AK Inflammation, fibrosis and cancer: Mechanisms, therapeutic options and challenges. Cancers 2022, 14 (3), 552. [PubMed: 35158821]

(45). Cotter TG; Rinella M Nonalcoholic fatty liver disease 2020: the state of the disease. Gastroenterology 2020, 158 (7), 1851–1864. [PubMed: 32061595]

(46). Cottin V; Richeldi L Neglected evidence in idiopathic pulmonary fibrosis and the importance of early diagnosis and treatment. Eur. Respir. Rev 2014, 23 (131), 106–110. [PubMed: 24591667]

(47). Hariri LP; Roden AC; Chung JH; Danoff SK; Gomez Manjarres DC; Hartwig M; Kheir F; King C; Kreider M; Lynch DA The role of surgical lung biopsy in the diagnosis of fibrotic interstitial lung disease: Perspective from the pulmonary fibrosis foundation. Ann. Am. Thorac. Soc 2021, 18 (10), 1601–1609. [PubMed: 34004127]

(48). Nandy S; Raphaely RA; Muniappan A; Shih A; Roop BW; Sharma A; Keyes CM; Colby TV; Auchincloss HG; Gaissert HA Diagnostic accuracy of endobronchial optical coherence tomography for the microscopic diagnosis of usual interstitial pneumonia. Am. J. Respir. Crit. Care Med 2021, 204 (10), 1164–1179. [PubMed: 34375171]

(49). Tapper EB; Loomba R Noninvasive imaging biomarker assessment of liver fibrosis by elastography in NAFLD. Nat. Rev. Gastroenterol. Hepatol 2018, 15 (5), 274–282. [PubMed: 29463906]

(50). Sanyal AJ; Shankar SS; Calle RA; Samir AE; Sirlin CB; Sherlock SP; Loomba R; Fowler KJ; Dehn CA; Heymann H Non-Invasive biomarkers of nonalcoholic steatohepatitis: the FNIH NIMBLE project. Nat. Med 2022, 28 (3), 430–432. [PubMed: 35145308]

(51). Desogere P; Tapias LF; Rietz TA; Rotile N; Blasi F; Day H; Elliott J; Fuchs BC; Lanuti M; Caravan P Optimization of a Collagen-Targeted PET Probe for Molecular Imaging of Pulmonary Fibrosis. J. Nucl. Med 2017, 58 (12), 1991–1996. [PubMed: 28611243]

(52). Desogere P; Tapias LF; Hariri LP; Rotile NJ; Rietz TA; Probst CK; Blasi F; Day H; Mino-Kenudson M; Weinreb P; et al. Type I collagen-targeted PET probe for pulmonary fibrosis detection and staging in preclinical models. Sci. Transl. Med 2017, 9 (384).

(53). Wahsner J; Desogere P; Abston E; Graham-O'Regan KA; Wang JF; Rotile NJ; Schirmer MD; Ferreira DD; Sui JY; Fuchs BC; et al. Ga-68-NODAGA-Indole: An Allysine-Reactive Positron Emission Tomography Probe for Molecular Imaging of Pulmonary Fibrogenesis. J. Am. Chem. Soc 2019, 141 (14), 5593–5596. [PubMed: 30908032]

(54). Izquierdo-Garcia D; Desogere P; Le Fur M; Shuvaev S; Zhou IY; Ramsay I; Lanuti M; Catalano OA; Catana C; Caravan P; et al. Biodistribution, Dosimetry, and Pharmacokinetics of 68Ga-CBP8: A Type I Collagen-Targeted PET Probe. J. Nucl. Med 2023, 64 (5), 775–781. [PubMed: 37116909]

(55). Montesi SB; Izquierdo-Garcia D; Desogere P; Abston E; Liang LL; Digumarthy S; Seethamraju R; Lanuti M; Caravan P; Catana C Type I Collagen-targeted Positron Emission Tomography Imaging in Idiopathic Pulmonary Fibrosis: First-in-Human Studies. Am. J. Respir. Crit. Care Med 2019, 200 (2), 258–261. [PubMed: 31161770]

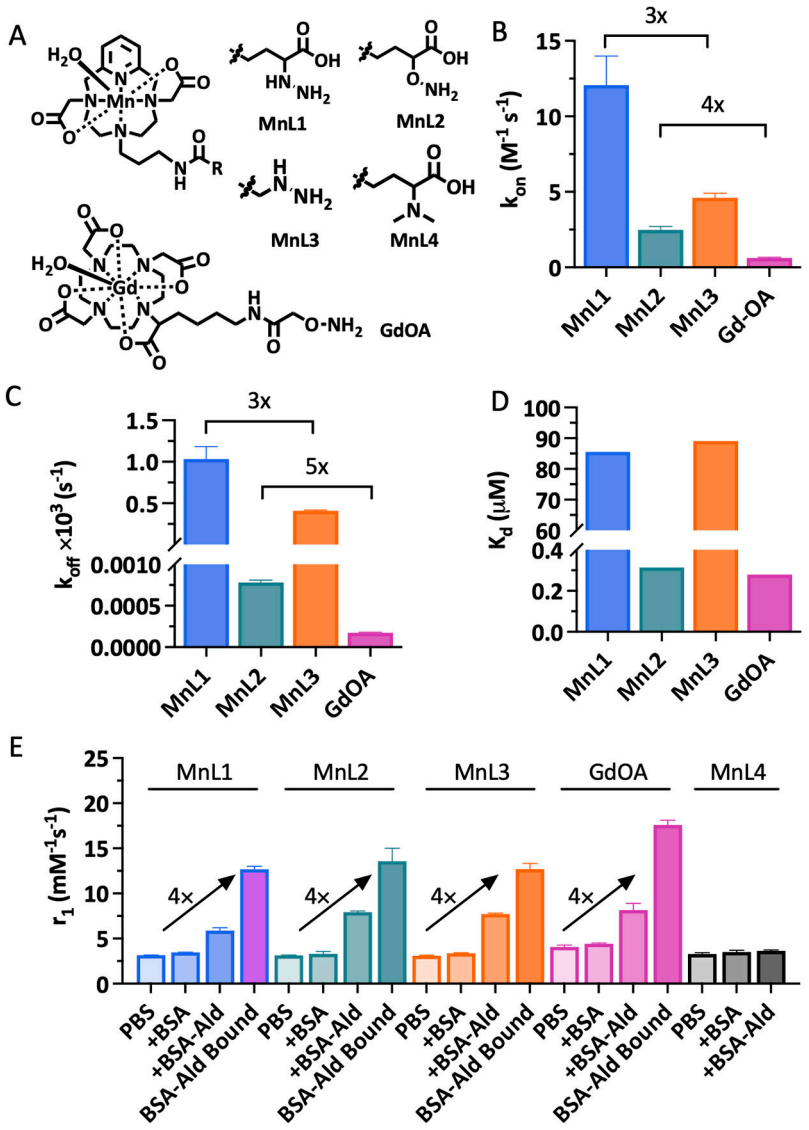


**Figure 1.**

Design and characterization of extracellular aldehyde-targeted MR probes. A, Structure of novel MnPC2A-based complexes and the known compound **GdOA**. B, Second order rate constant ($k_{on}$) for the reaction of **MnL1**, **MnL2**, **MnL3**, and **GdOA** with butyraldehyde (pH 7.4, PBS, 25 °C; data presented as mean ± s.d., n = 3 independent samples). C, Hydrolysis rate constant ($k_{off}$) of condensation products (data presented as mean ± s.d., n = 3 independent samples). D, Dissociation constant ($K_d$) of condensation reaction between hydrazine/oxyamine-based probes with butyraldehyde calculated as the ratio $k_{off}/k_{on}$. E, Relaxivities of **MnL1**, **MnL2**, **MnL3**, **MnL4**, and **GdOA** in PBS, in BSA, in allysine-modified BSA-Ald, and of the BSA-Ald bound species (1.4 T, 37°C. Data presented as mean ± s.d., n = 3 independent samples).

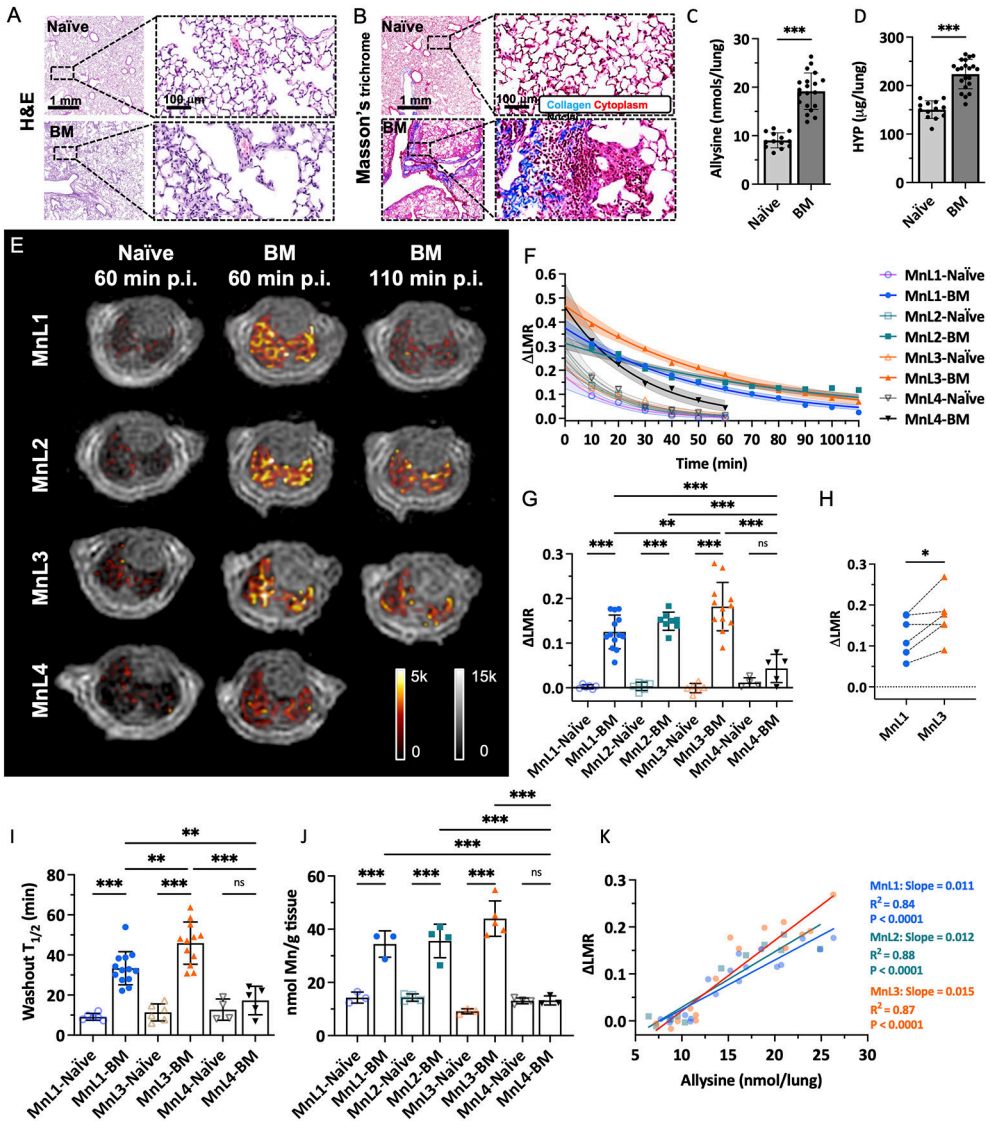


**Figure 2.**

Molecular MRI of bleomycin-induced lung fibrogenesis. Representative H&E (A) and Masson's trichrome (B) staining of lung section from naïve and BM mice. Bleomycin-injured lung showed increased tissue density, cellularity, and collagen deposition compared with normal lungs. Lung allysine (C) and hydroxyproline (HYP) (D) content were significantly increased in BM mice compared with naïve mice. Data presented as mean ± s.d.; n = 13 for naïve mice, n = 20 for BM mice). Statistical analysis was performed using two-tailed unpaired Student's *t* test, unpaired, ** $p < 0.01$, *** $p < 0.001$). E, Representative lung enhancement in naïve and BM mice. Coronal UTE images overlaid with false color image of lung enhancement generated by subtraction of the pre-injection UTE image from post-injection UTE image. **MnL1**, **MnL2**, and **MnL3** produced higher signals in BM mice lungs than in naïve mice and higher signal in **MnL4** injected naïve and BM mice at 60 min post-injection. F, Change of lung-to-muscle ratio (ΔLMR) as a function of time in naïve and BM mice after injection of **MnL1**, **MnL2**, **MnL3**, and **MnL4**. Data are

presented as mean value with 95% simultaneous confidence bands as shaded regions; Naïve mice: n = 6 for **MnL1**, **MnL2**, and **MnL3**, n = 4 for **MnL4**; BM mice: n = 13 injected with **MnL1**, n = 8 injected with **MnL2**, n = 12 injected with **MnL3**, and n = 5 injected with **MnL4**. G, Image quantification of ΔLMR in lungs of naïve and BM mice 60 min post-injection of **MnL1**, **MnL2**, **MnL3**, and **MnL4**. Hydrazine/oxyamine bearing probes exhibited specific lung signal enhancement in the fibrotic lung. Data presented as mean ± s.d. Statistical analysis was performed using one-way ANOVA with Tukey's post hoc test, **P < 0.01, ***P < 0.001, ns not statistically significant). H, Pair-wise analysis of ΔLMR in bleomycin-injured mice at 60 min post-injection of **MnL1** and **MnL3** (n = 6). Statistical analysis was performed using two-tailed paired Student's *t* test, *P < 0.05. *I*, Washout $T_{1/2}$ of **MnL1**, **MnL3**, and **MnL4** in naïve and BM mice. **MnL3**, with higher hydrazone hydrolytic stability, exhibited longer residence time in fibrotic lungs. Data presented as mean ± s.d.; Naïve mice: n = 6 for **MnL1**, and **MnL3**, n = 4 for **MnL4**; BM mice: n = 13 injected with **MnL1**, n = 12 injected with **MnL3**, and n = 5 injected with **MnL4**. Statistical analysis was performed using one-way ANOVA with Tukey's post hoc test, *P < 0.05, ***P < 0.001, ns not statistically significant. J, Quantification of Mn content in the left lungs of naïve and BM mice 60 min after injection of **MnL1**, **MnL2**, **MnL3**, and **MnL4**. Injection of hydrazine/oxyamine-bearing probes produced significantly higher Mn concentrations in the fibrotic lung compared with normal lung. No preferential uptake was observed in naïve or BM mice injected with **MnL4**. Data are presented as mean ± s.d.; Naïve mice: n = 3 for **MnL1**, n = 4 for **MnL2**, n = 3 for **MnL3**, n = 4 for **MnL4**; BM mice: n = 3 for **MnL1**, n = 4 for **MnL2**, n = 5 for **MnL3**, n = 3 for **MnL4**. Statistical analysis was performed using one-way ANOVA with Tukey's post hoc test, *P < 0.05, **P < 0.01, ***P < 0.001, ns not statistically significant. K, The MRI lung signal enhancement in naïve and BM mice imaged with **MnL1**, **MnL2**, and **MnL3** correlates well with allysine content. Compared with **MnL1**, **MnL3** exhibited higher sensitivity in detecting fibrogenesis ($slope_{MnL1}$ = 0.011 vs. $slope_{MnL3}$ = 0.015).

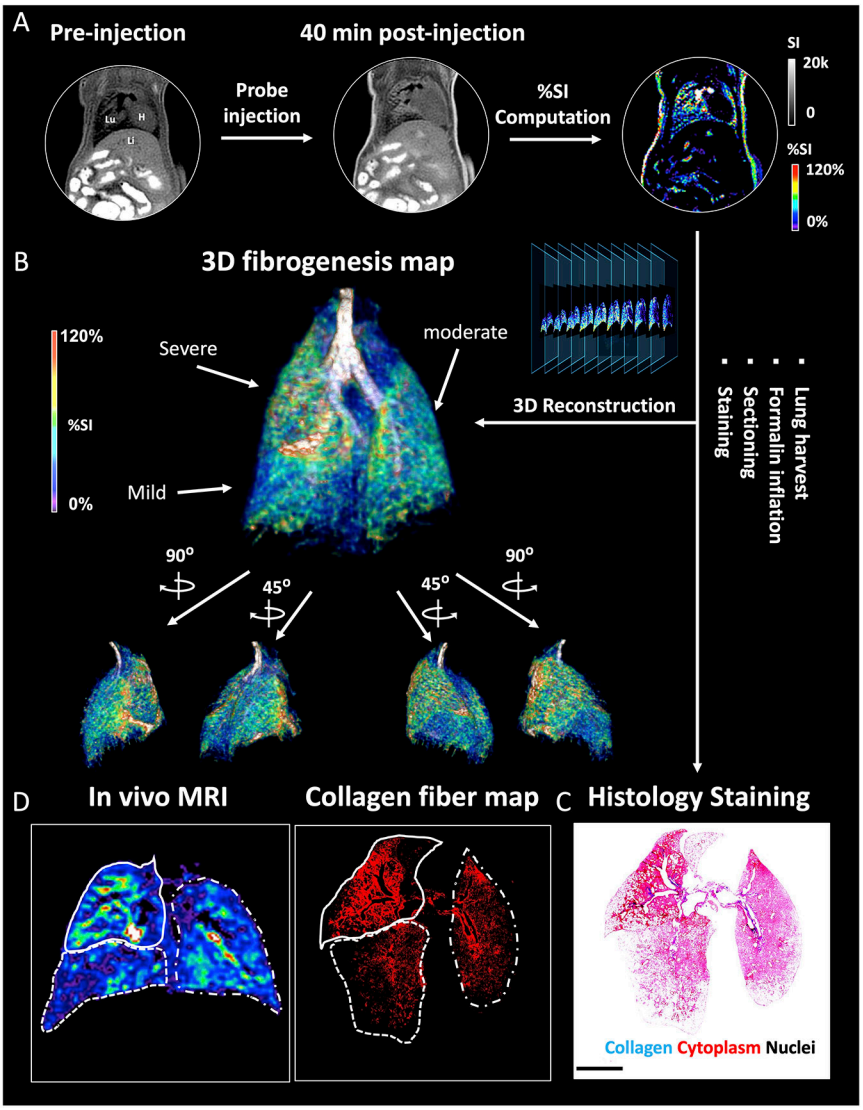


**Figure 3.**

3D mapping of lung fibrogenesis and histology validation. A, Representative UTE images of BM mouse pre- and 40 min post-injection of MnL3 were acquired and a pixelwise signal enhancement map was generated (Lu: lung; Li: liver; H: heart). B, 3D whole lung fibrogenesis MR map of the fibrotic lung. C, Masson's Trichrome staining. After in vivo imaging, the lung was harvested, fixed, serially sectioned, and stained was performed to validate the MR images. D, In vivo MRI signal enhancement exhibited the same fibrotic distribution pattern compared to ex vivo histology.

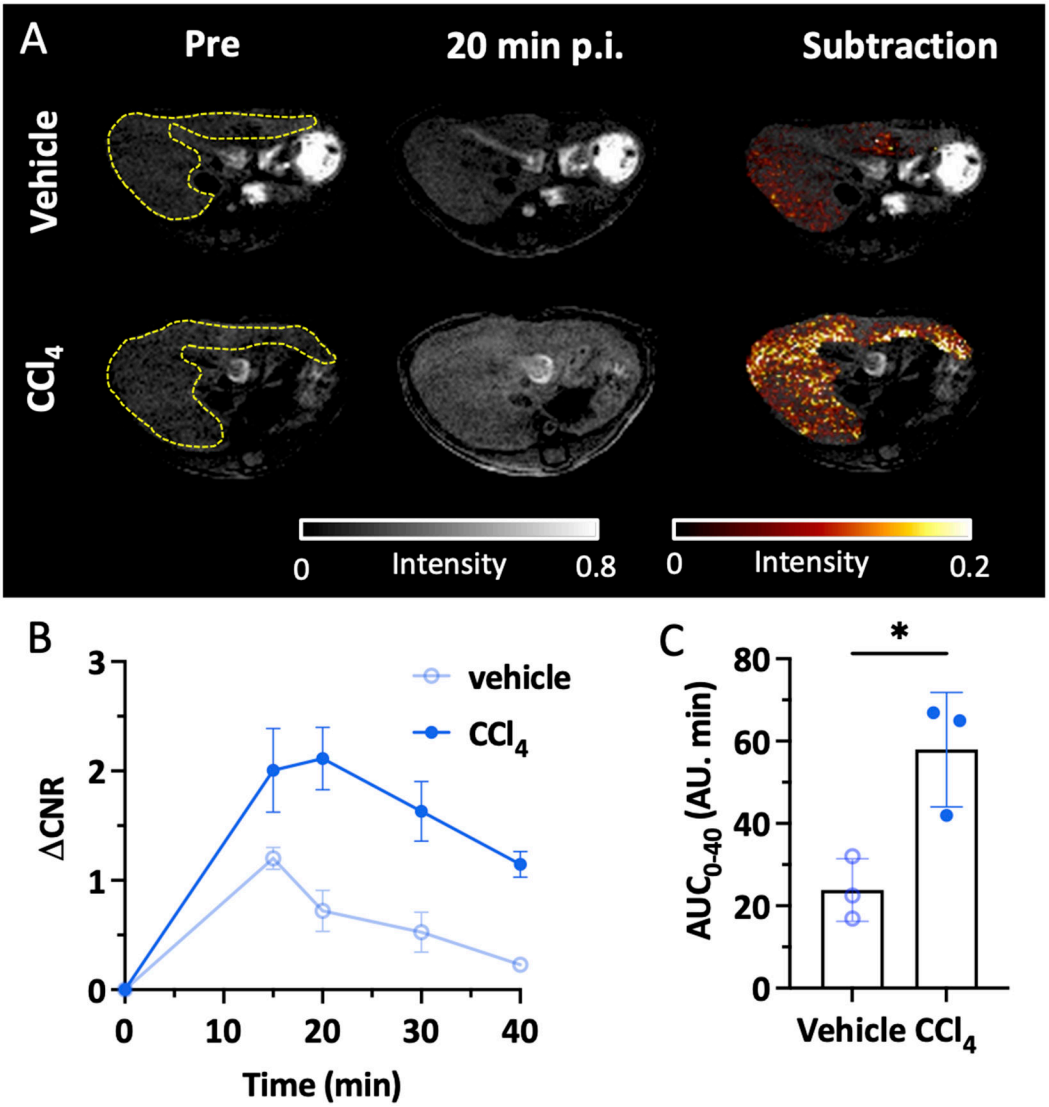


**Figure 4.**

Molecular MRI of hepatic fibrogenesis. A, Representative axial MR images showing the livers of mice that received olive oil vehicle (top row) or $CCl_4$ (bottom row) for 12 weeks; left: image before **MnL1** administration, middle 20 min post-injection of **MnL1**, and right subtraction of post – pre injection image. B, Change in liver-to-muscle contrast to noise ratio ($\Delta CNR = CNR_{Post} - CNR_{Pre}$) of vehicle-treated and $CCl_4$ mice as a function of time following i.v. injection of **MnL1** (Data presented as mean ± s.d.; n = 3 for each group). C, Significant difference in the area under the ΔCNR curve ($AUC_{0\text{-}40}$) between vehicle and $CCl_4$ mice. Data presented as mean ± s.d.; n = 3 for each group; Statistical analysis was performed using two-tailed unpaired Student's *t* test, two-tailed unpaired, *P < 0.05.

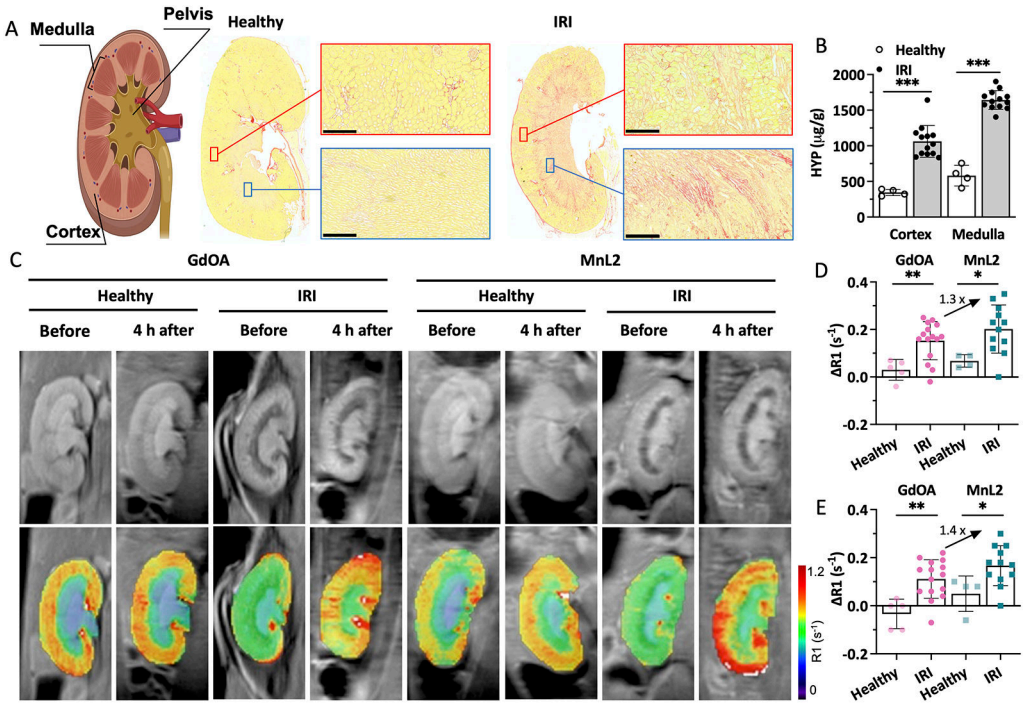


**Figure 5.**

Molecular MRI of renal fibrogenesis. A, Left: schematic of anatomy of kidney; middle: Sirius Red stained kidney section from a naïve mouse (healthy); right: Sirius Red stained kidney section from a kidney with ischemia-reperfusion injury (IRI) 14 days prior (collagen: red, normal tissue yellow; scale bar:250 μm). IRI kidney showed increased collagen in the cortex and medulla compared with the healthy kidney. B, IRI kidneys showed significantly higher hydroxyproline concentration in the cortex and medulla compared to healthy kidneys. Data are presented as mean ± s.d.; n = 13 for IRI kidney, n = 4 for healthy kidney. Statistical analysis was performed using Student's *t* test, two-tailed, *** $p < 0.001$. C, Representative mouse MR images showing kidneys of healthy mice and mice 14 days post-IRI. Images are shown before and 4 hours after injection of **GdOA** or **MnL2**. Top row shows greyscale kidney anatomy MR image and bottom row shows R1 maps calculated from inversion recovery images. D, Quantification of ΔR1 (R1(4 h post) – R1(pre)) in cortex of healthy and IRI injured mice administered **GdOA** or **MnL2**. **MnL2** and **GdOA** exhibited similar low ΔR1 values in healthy mice, but both probes showed significantly higher ΔR1 values in the IRI kidney. **MnL2** with a higher condensation reaction rate constant compared to **GdOA**, resulting in higher ΔR1 than **GdOA** in the IRI kidney. Data are presented as mean ± s.d.; Naïve healthy mice: n = 5 for **GdOA**, n = 4 for **MnL2**; IRI mice: n = 15 for **GdOA**, n = 11 for **MnL2**. Statistical analysis was performed using two-tailed unpaired Student's *t* test, unpaired, *$P < 0.05$, **$P < 0.01$. E, Quantification of ΔR1 (R1(4 h post) – R1(pre)) in medulla of healthy and IRI mice administered **GdOA** or **MnL2**. **MnL2** and **GdOA** exhibited similar low ΔR1 values in healthy mice, but both probes showed significantly higher ΔR1 values in the IRI kidney. **MnL2** with a higher condensation reaction rate constant compared to **GdOA**, resulting in higher ΔR1 than **GdOA** in the IRI kidney. Data are presented as mean ± s.d.; Naïve healthy mice: n = 5 for **GdOA**, n = 4 for **MnL2**;

IRI mice: n = 15 for **GdOA**, n = 11 for **MnL2**. Statistical analysis was performed using two-tailed unpaired Student's *t* test, unpaired, *P < 0.05, **P < 0.01.